GLCM FEATURES FOR LEARNING FLOODED VEGETATION FROM SENTINEL-1 AND SENTINEL-2 DATA

Beste Tavus[1,2], Sultan Kocaman [2*]

[1] Hacettepe University, Graduate School of Science and Engineering, Ankara, Turkey - beste.tavus@hacettepe.edu.tr
[2] Hacettepe University, Department of Geomatics Engineering, 06800 Beytepe Ankara, Turkey - sultankocaman@hacettepe.edu.tr

KEY WORDS: Flood Mapping, Inundated (Flooded) Vegetation, Random Forest, GLCM, Sentinel-1, Sentinel-2

ABSTRACT:

Efforts on flood mapping from active and passive satellite Earth Observation sensors increased in the last decade especially due to the availability of free datasets from European Space Agency's Sentinel-1 and Sentinel-2 platforms. Regular data acquisition scheme also allows observing areas prone to natural hazards with a small temporal interval (within a week). Thus, before and after datasets are often available for detecting surface changes caused by flooding. This study investigates the contribution of textural variables to the predictive performance of a data-driven machine learning algorithm for detecting the effects of a flooding caused by Sardoba Dam break in Uzbekistan. In addition to the spectral channels of Sentinel-2 and polarization bands of Sentinel-1, two spectral indices (normalized difference vegetation index and modified normalized difference water index), and textural features of gray-level co-occurrence matrix (GLCM) were used with the Random Forest. Due to high dimensionality of input variables, principal component (PC) analysis was applied to the GLCM features and only the most significant PCs were used for modeling. The feature stacks used for learning were derived from both pre- and post-event Sentinel-1 and Sentinel-2 images. The models were validated through model test measures and external reference data obtained from PlanetScope imagery. The results show that the GLCM features improve the classification of flooded areas (from 82% to 93%) and flooded vegetation (from 17% to 78%) expressed in user's accuracy. As an outcome of the study, the use of textural features is recommended for accurate mapping of flooded areas and flooded vegetation.

1. INTRODUCTION

Flood events, the frequency and severity of which are increasing because of urbanization and population growth, cause devastating effects on society, economy and ecosystems worldwide (EMDAT, 2022). It is essential to produce reliable spatial and temporal information on the extent of the flood in order to mitigate their impacts and to plan the disaster management, emergency response and insurance processes effectively. In this context, the potential of widely used Earth Observation (EO) datasets and various mapping approaches in identifying smooth open water bodies and flooded areas has been proven in many studies (e.g., see Tavus et al., 2018, 2019 2020, 2022; Bentivoglio et al., 2022; Cerbelaud et al., 2021).

In most flooding hazard events in rural areas, inundated vegetation accounts for more than three-quarters of the total flooded area. In this context, many approaches that rely on backscattering intensity have been used in the literature for the determination of inundated vegetation. Betbeder et al. (2014) evaluated multitemporal TerraSAR-X horizontal-horizontal (HH) and vertical-vertical (VV) polarizations and polarimetric parameter, the Shannon entropy (SE), by using support vector machine (SVM), K-nearest neighbors and decision tree (DT) algorithms to identify vegetation types under the flood event. In the study, the classification results reached the highest kappa index of 0.85 and the contribution of polarimetric parameters to the results was compared with the HH, VV or combined (HH and VV) backscatter parameters. Accordingly, it was emphasized that the use of polarimetric parameters contributed to the determination of inundated vegetation. Cazals et al. (2016) evaluated the potential of Sentinel-1 VV and HV polarizations by using a backscatter thresholding algorithm to detect open water, flooded vegetation and non-flooded grassland. In the study, open water was successfully detected, but flooded grasslands were detected with a poor accuracy level because of the fine-grained grass/crops patterns.

In approaches based on backscatter analysis, polarimetric synthetic aperture radar (PolSAR) and interferometric SAR (InSAR) coherence are preferred to minimize the confusion of inundated vegetation with urban areas and shadow areas with open water (Brisco et al. 2013; Gallant et al., 2014; Dabboor et al., 2015; Plank et al., 2017; Tavus et al., 2022). Plank et al. (2017) presented a procedure specifically focusing on the identification of inundated vegetation based on C-band Sentinel-1 and L-band ALOS-2/PALSAR-2 data. As a result of the proposed procedure involving polarimetric decomposition, it was emphasized that the C band data (Sentinel-1) is suitable for smooth water detection, while L band (ALOS-2/PALSAR-2) data provides detailed information about flooded vegetation. Brisco et al. (2019), analyzed the RADARSAT HH and HV polarizations to map flooded vegetation, noting that the polarizations were less effective for this purpose due to increase of backscatter intensity and phase shift from double bounce scattering. The polarization ratio (HH/HV), Shannon entropy and m-chi decomposition provided a good discrimination between flooded vegetation and the other class.
In summary, while decomposition methods such as Sinclair, Freeman–Durden, Yamaguchi, H-α Alpha, etc. provide higher

* Corresponding author

discrimination ability on backscattering characteristics of objects, coherency data evaluated based on seasonality allows determination of flooded vegetation. However, there are limitations to the application of these methods in terms of the availability of full polarimetric data, area coverage, temporal and geometric resolution (Tsyganskaya et al., 2019).

In recent years, the studies in the literature aiming to determine the flooded vegetation have focused on the use of the complementary potential of SAR and optical data together. In this context, Sentinel-1 SAR and Sentinel-2 optical datasets are preferred due to their temporal and spatial resolutions. Studies using only Sentinel-2 (Bhatnagar et al., 2018) and jointly using Sentinel-1&2 (Chatziantoniou et al., 2017; Nhangumbe et al., 2023) have demonstrated benefits of both datasets for flood mapping. In addition, there are many studies investigating the potential of multi-temporal Sentinel-1 (Huang et al., 2017; Mleczko and Mróz, 2018; Tsyganskaya et al., 2018) and Sentinel-2 (Ludwig et al., 2019) datasets.

A recent study by Tavus et al. (2022) evaluated accurate flood mapping potential of Sentinel-1 and Sentinel-2 datasets comprehensively by comparing the different data availability scenarios, such as only pre- event Sentinel-2 together with pre- and post-event Sentinel-1, or the use of only Sentinel-1, etc. The study area was in Sirdaryo region of Uzbekistan, in which a dam break occurred on May 1st 2020 and caused flooding over a large region known for its high agricultural activity. The results obtained from the random forest (RF) classification revealed that the highest accuracy could be obtained by using both the pre- and post-event Sentinel 1&2 data and a set of hand-crafted feature set, such as spectral indices and textural variables.

This study aimed at providing an in-depth analysis on the contribution of textural features for classification accuracy explicitly. For this purpose, we produced gray-level co-occurrence matrix (GLCM) textural features and assessed their capability for learning inundated vegetation from Sentinel-1 and Sentinel-2 imagery. In this context, a multi-temporal feature space was created by generating pre- and post-event GLCM textures and various spectral indices. The feature spaces with and without GLCM variables were than used for modeling with the RF classifier. The results were validated using information obtained from the PlanetScope orthoimage with 3 m spatial resolution. The data, methods and results are presented and discussed here.

2. MATERIALS AND METHODS

Under the following sub-headings, the study area, the data and the methodology are described in detail.

2.1 Study Area and Datasets

The Sardoba Dam was built between 2010-2017 on the Syr Darya River in Uzbekistan. Completed in 2017, the dam reservoir was designed to hold more than ~922 million m^3 of water to irrigate the fertile farmland around the region, where crops such as cotton and wheat are usually produced (Simonow, 2020). On May 1, 2020, the region was flooded due to a break on the wall of the dam. The flood waters advanced into the borders of Kazakhstan and caused destruction in a wide area consisting of settlements and fertile crop lands.

The location of the study area and the corresponding land use land cover (LULC) map are illustrated in Figure 1. The study area spans around 2009 km^2 and, as per the ESA WorldCover product, comprises 69.8% cropland, 16.6% bare/sparse vegetation, 6.2% urban area, 4.9% grassland, and 2.1% permanent water bodies (ESA-WorldCover, 2020).

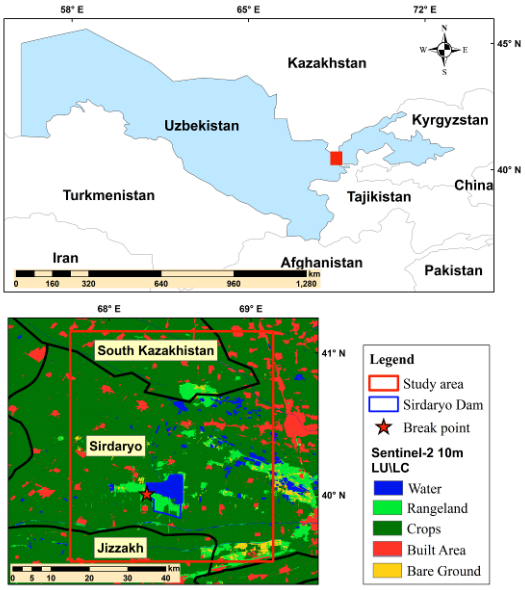

Figure 1. The study site location (above) and the LULC map obtained from the ESA WorldCover (below).

In this study, we utilized Sentinel-1 and Sentinel-2 datasets provided by the ESA Copernicus Programme (Copernicus, 2020). Table 1 summarizes the data properties and the ground conditions at the time of the data acquisition, such as pre- or post-event. The selected Sentinel-1 and Sentinel-2 data accurately represented the pre-and post-flood conditions. Figure 2 displays the pre-and post-flood Sentinel-2 RGB images acquired on April 24 and May 04, 2020, respectively, together with Sentinel-1 VV polarization images. Additionally, validation datasets were generated using PlanetScope orthoimages with 3 m spatial resolution. For this purpose, we manually delineated reference polygons of each class from PlanetScope data acquired on May 10, 2020, through the Planet Explorer platform (www.planet.com).

	Acquisiton Date	Condition	Usage
Sentinel-1	2020/04/29 2020/05/25	Pre-event Post-event	Feature generation & Classification
Sentinel-2	2020/04/24 2020/05/04	Pre-event Post-event	Feature generation & Classification
PlanetScope orthoimage	10/05/2020	Post-event	External reference for Validation

Table 1. Basic specifications of the datasets used in the study.

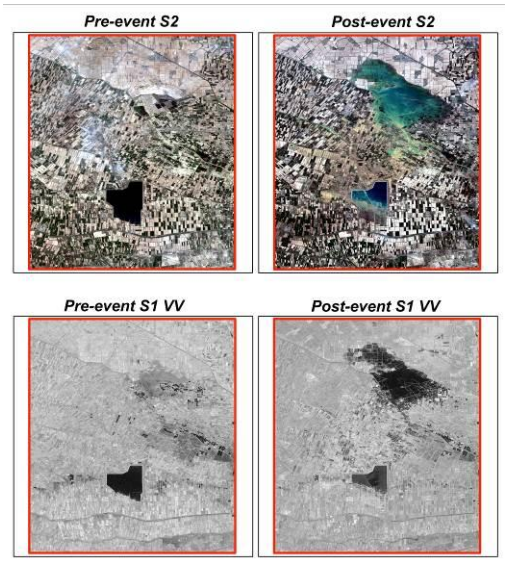

Figure 2. Satellite images of the study site obtained from Sentinel-2 and the VV polarization data of Sentinel-1.

2.2 Methodology

The methodology of this study consists of three basic stages as *(i)* data pre-processing and feature extraction, *(ii)* feature selection, and *(iii)* modeling, mapping and validation, as depicted in Figure 3. In the first stage of data pre-processing and feature extraction, several methods such as noise filter and removal of systematic errors caused by terrain were applied to the Sentinel-1 data. The lower resolution band of Sentinel-2 (B11) was upsampled as well. The normalized difference vegetation index (NDVI) and modified normalized difference water index (MNDWI) spectral indices were produced from the pre- and post-event Sentinel-2 data. In addition, a total of 10 GLCM texture variables introduced by Haralick et al. (1973) were applied to each of the pre-event and post-event Sentinel-1 and Sentinel-2 band data.

In the second stage, Principle Component Analysis (PCA) was applied to the GLCM variables produced for the pre- and post-event Sentinel-1 and Sentinel-2 data in order to reduce the dimensionality as there were a total of 140 of them. A total of 12 GLCM principle components (GLCM PCs) obtained from the analysis were used as additional information to the original Sentinel-1 (S1) and Sentinel-2 (S2) bands. This dataset (Stack-1) involving the GLCM PCs produced in the study by Tavus et al. (2022) was used for the modelling with the RF classifier, and the results were validated with a test dataset (546.052 reference samples) produced from an external reference (PlanetScope orthoimages). The bands included in Stack-1 are pre- and post-event S1 VV, S1 VH, S1 GLCM PCs, 5 bands of S2 (B2, B3, B4, B8, B11), S2 GLCM PCs, NDVI and MNDWI.

In order to assess the contribution of the GLCM feature components (GLCM PCs) to the prediction of flooded areas and flooded vegetation, these features were removed from the Stack-1 dataset to obtain Stack-2, which consists of pre- and post-event S1 VV, S1 VH, 5 bands of S2 (B2, B3, B4, B8, B11), NDVI and MNDWI. The training data was manually delineated on the S2 RGB imagery for the Stack-1, and was also used for the learning process with Stack-2.

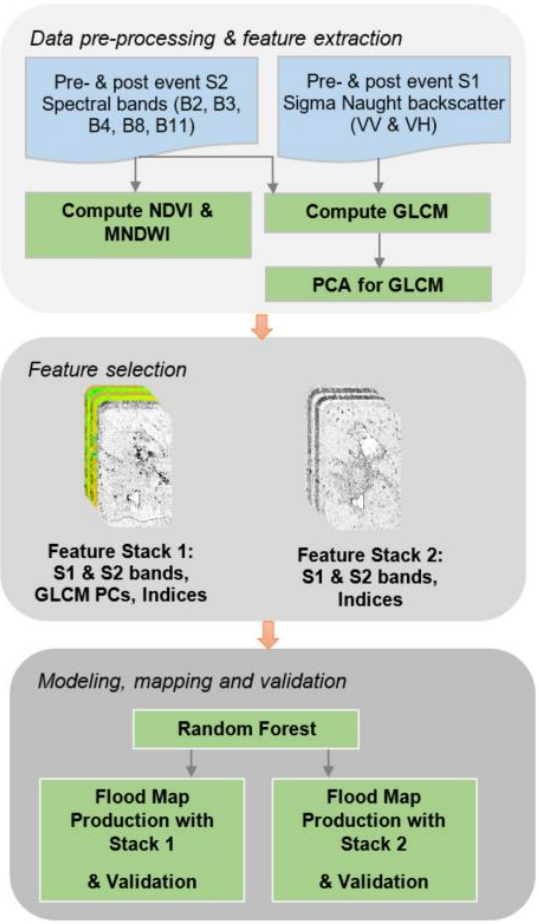

Figure 3. Overall methodology of the study.

In the third stage, the RF method proposed by Breiman (2001), which is based on decision trees, was used for learning from data formed in the previous stage. A total of seven LULC classes, namely flooded vegetation (FV), flooded area (FL), bare land (BL), permanent water (PW), urban area (Ur), vegetation 1 (V1) and vegetation 2 (V2), were identified from the post-event Sentinel-2 images. For this, a total of 13.539 training samples manually delineated from post-event Sentinel-2 were used with a tree size of 300 and 3-fold cross-validation. Previous studies carried out by Tavus et al. (2018, 2020, 2022) have shown that instead of applying a binary classification approach for flooded areas, applying a holistic LULC classification increases the accuracy and reliability of flood extent maps. Thus, the seven classes mentioned above were defined in the modeling with Stack-1 and Stack-2. The results were tested using pixels inside the test polygons identified on the external reference imagery of PlanetScope for both feature stacks.

3. RESULTS AND DISCUSSIONS

Figure 4 (a and b) shows the classification results for the seven classes as explained in the previous section. The distribution of the training polygons can also be seen in the figure. The flood maps obtained from the Stack-1 and Stack-2 exhibit differences especially in the FL, Ur and V1 classes, and even more in the FV class based on the visual inspection. No significant change was observed in the PW and V2 classes. Detailed views from the maps focusing rather on the FL and FV classes are given in

Figure 5 together with the test polygons delineated on the PlanetScope orthoimages. The extent of the maps shown in Figure 5 is illustrated with dashed black rectangle in Figure 4. Tables 2 and 3 represent the validation results as confusion matrices between the different classes for Stack-1 and Stack-2 predictions, respectively. In the tables, the rows and the columns represent the numbers of actual (PlanetScope) and the predicted class samples, respectively. As can be seen in the tables, 86% overall accuracy (OA) and 83% Kappa (K) values were obtained as a result of Stack-1 classification, while 68% OA and 60% K values were obtained as a result of Stack-2 classification. In addition, Table 4 provides further accuracy measures comparatively for both stacks, such as the producer's accuracy (PA) or omission error, and user's accuracy (UA) or commission error.

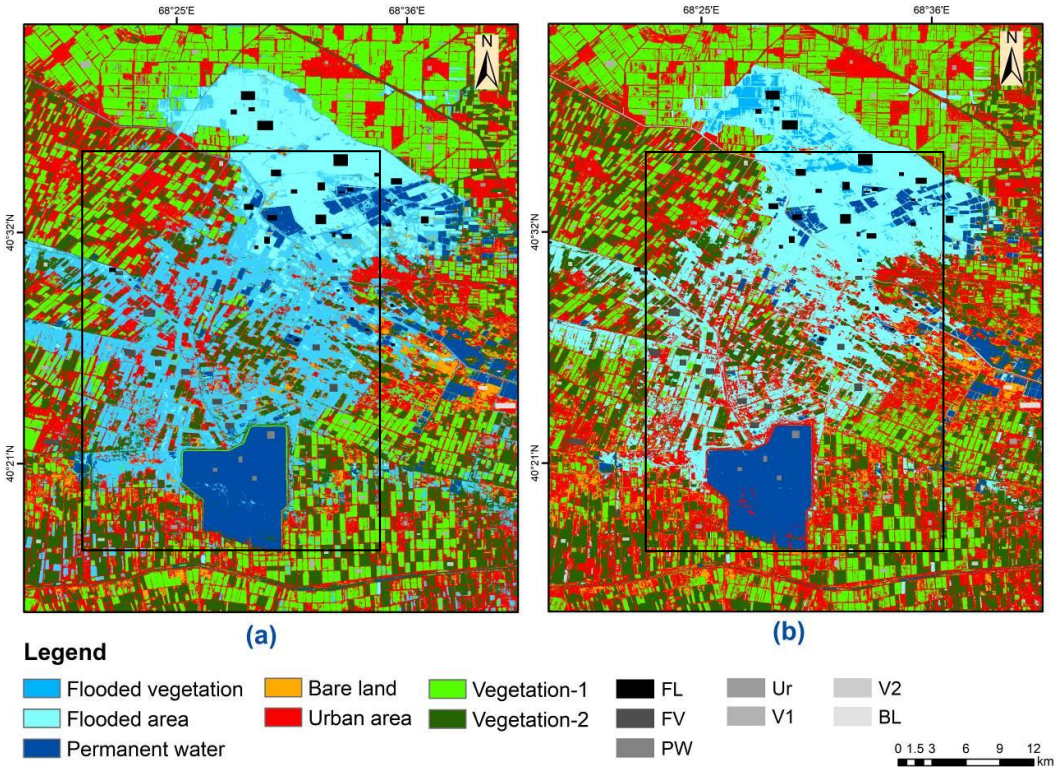

Figure 4. The RF classification results obtained from (a) Stack-1 (pre- and post-event S1 VV & VH & GLCM PCs & pre- and post-event S2 GLCM PCs & NDVI & MNDWI) and (b) Stack-2 (pre- and post-event S1 VV & VH & pre- and post-event S2 & NDVI & NMDWI). Polygons FL, FV, PW, Ur, V1, V2 and BL, shown in black-white tones, represent the training dataset.

	BL	**FL**	**FV**	**PW**	**Ur**	**V1**	**V2**
BL	11131	2916	1478	0	6497	623	2662
FL	502	88754	2325	58	846	2300	333
FV	386	10053	107663	19808	2	0	129
PW	0	0	0	75841	0	0	37
Ur	802	8045	27	91	53554	4722	1507
V1	239	1902	0	0	4617	111129	2
V2	29	0	0	0	4217	0	20825
Overall accuracy (OA): 86% Kappa(K): 83%							

Table 2. Confusion matrix obtained from the RF classification of Stack-1 and the accuracy measures.

	BL	**FL**	**FV**	**PW**	**Ur**	**V1**	**V2**
BL	10048	2965	0	0	12157	123	14
FL	157	78404	1	2	8525	7378	651
FV	2	101018	23238	13591	152	0	40
PW	0	92	0	75611	175	0	0
Ur	403	2701	0	73	61186	1429	2956
V1	63	395	0	0	15934	101467	30
V2	13	0	0	0	4196	0	20862
Overall accuracy (OA): 68% Kappa(K): 60%							

Table 3. Confusion matrix obtained from the RF classification of Stack-2 and the accuracy measures.

	BL	FL	FV	PW	Ur	V1	V2
PA (%) Stack1 / Stack2	85/94	**79/42**	96/99	79/85	**77/60**	94/92	82/85
UA (%) Stack1 / Stack2	44/40	**93/82**	**78/17**	100/99	78/89	**94/86**	83/83

Table 4. PA and UA accuracy metrics obtained from the RF classifications with Stack-1 and Stack-2.

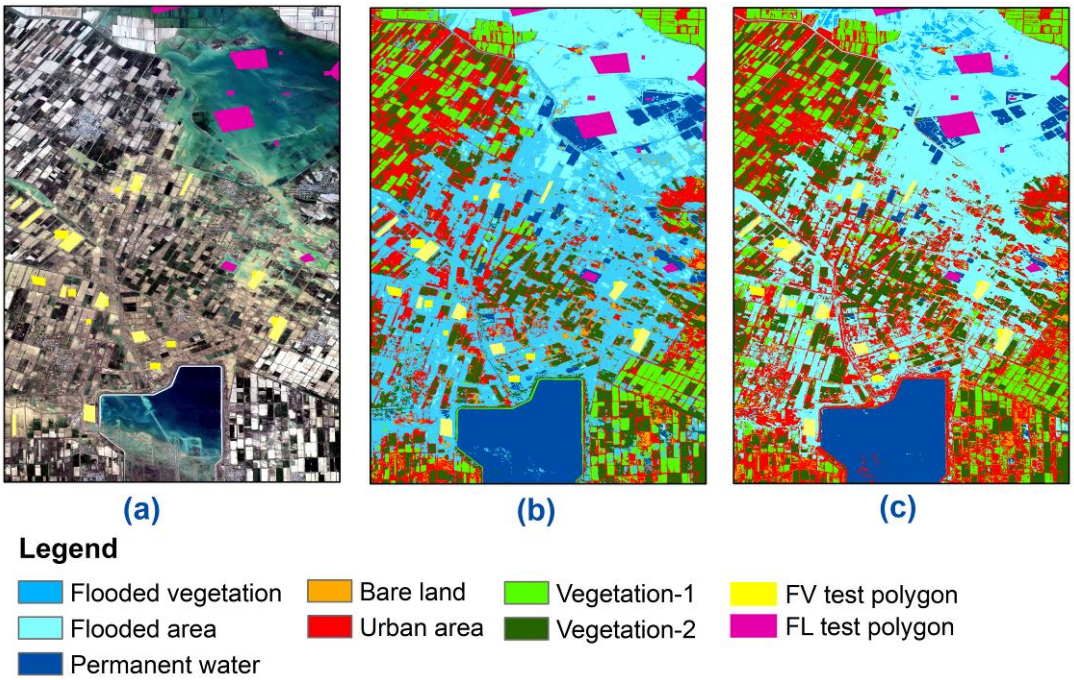

Figure 5. Detailed views from the FV and FL polygons as a part of reference data in (a) Sentinel-2 post-event RGB image, (b) flood map with GLCM features (Stack-1), (c) flood map without GLCM features (Stack-2).

As can be seen from the Tables 2 and 3, with the use of GLCM, the OA value increased from 68% to 86%, and the K value increased from 60% to 83%. According to Table 4, with the use of GLCM, the PA of the FL class increased from 42% to 79%, while the UA increased from 82% to 93%. Based on the bold marked values in Table 4, it can be concluded that the utilization of GLCM has a great impact on the learning of the FL, FV, Ur, and V1 classes in this study.

As seen in both the classification results and the error matrices, the use of GLCM data significantly contributes to increasing the classification accuracy by preventing the mixture between the FV and FL classes. When GLCM is not used, more than 3/4 of the FV class was mislabelled as FL, whereas no mixing occurs between the FV and the other classes. In other words, the missing textural variables resulted in the misclassification of flood areas as urban and vegetation. It is evident that the inundated vegetation shows a different scattering mechanism in radar data compared to other classes. This particularly finding highlights the difference in texture properties of the inundated vegetation compared to the floods, water, or the other agricultural areas in the region.

Although the use of GLCM PCs has increased the PA of the urban areas from 60% to 77%, the UA has decreased from 89% to 78% since Ur class pixels were labeled as FL. Therefore, it can be said that the texture information causes complexity during the learning of Ur and FL classes. Also, comparison of both sets of results showed that the PA of the PW class which classified with GLCM has increased from 79% to 85%. The PA values of the PW class were 79% and 85% in Stack-1 and Stack-2, respectively. Accordingly, the texture information caused more mixing between PW and FL classes. This situation is likely to be due to the mixing of the texture features that may occur on smooth water surfaces due to wave and/or wind effects with the PW class.

4. CONCLUSIONS AND FUTURE WORK

In the present study, the contribution of GLCM textural features for flood extent mapping including flooded vegetation were evaluated with the RF classifier applied to the learning set obtained from various Sentinel-1 polarization and Sentinel-2 spectral bands. The study area was located in the Uzbekistan-Syrdarya region, has been affected by dam flooding, and comprises 70% cropland. Besides several other factors, the site was selected as cloud-free Sentinel-2 images were available representing the post-event status and the topography is rather flat, thus the radar geometric distortions such as shadow can be neglected. Two sets of learning variables, one containing GLCM textural information in the form of principal components and the other one without GLCM textures were produced. A LULC classification for a total of seven classes were followed here. The results were assessed using external reference obtained from PlanetScope orthoimages with 3 m spatial resolution.

The results showed the use of GLCM PCs greatly contributed to increase the overall classification accuracy (OA= 86% with GLCM and OA=68% without GLCM) based on external reference. The UA of flooded vegetation class exhibited the highest improvement, from 17% to 78% without and with GLCM, respectively. The classification accuracy of the flooded areas also increased yielding an increase from 42% to 79% in terms of PA. Thus, the use of textural features is highly recommended for detecting both the flooded areas and the flooded vegetation.

On the other hand, the use of texture data has led to the misclassification of surfaces without texture, such as open water surfaces. Further strategies can be integrated to reduce this effect as future work.

ACKNOWLEDGEMENTS

This study is part of the Ph.D. thesis research of Beste Tavus.

REFERENCES

Betbeder, J., Rapinel, S., Corpetti, T., Pottier, E., Corgne, S., Hubert-Moy, L. 2014. Multitemporal classification of TerraSAR-X data for wetland vegetation mapping. Journal of applied remote sensing, 8(1), 083648-083648. https://doi.org/10.1117/1.JRS.8.083648

Bentivoglio, R., Isufi, E., Jonkman, S.N., Taormina, R. 2022. Deep learning methods for flood mapping: a review of existing applications and future research directions. Hydrology and Earth System Sciences, 26(16), 4345-4378. https://doi.org/10.5194/hess-26-4345-2022, 2022.

Bhatnagar, S., Ghosh, B., Regan, S., Naughton, O., Johnston, P., Gill, L. 2018. Monitoring environmental supporting conditions of a raised bog using remote sensing techniques. Proc. IAHS 380, 9–15. https://doi.org/10.5194/piahs-380-9-2018.

Breiman, L., 2001. Random forests. Machine Learning, 45(1), 5-32.

Brisco, B., Li, K., Tedford, B., Charbonneau, F., Yun, S., Murnaghan, K. 2013. Compact polarimetry assessment for rice and wetland mapping. International Journal of Remote Sensing, 34(6), 1949-1964. https://doi.org/10.1080/01431161.2012.730156

Brisco, B., Shelat, Y., Murnaghan, K., Montgomery, J., Fuss, C., Olthof, I., Hopkinson, C., Deschamps, A., Poncos, V. 2019. Evaluation of C-Band SAR for Identification of Flooded Vegetation in Emergency Response Products. Canadian Journal of Remote Sensing, 45(1), 73-87. https://doi.org/10.1080/07038992.2019.1612236

Cazals, C., Rapinel, S., Frison, P.L., Bonis, A., Mercier, G., Mallet, C., Corgne, S., Rudant, J.-P. 2016. Mapping and Characterization of Hydrological Dynamics in a Coastal Marsh Using High Temporal Resolution Sentinel-1A Images. Remote Sensing, 8, 570. https://doi.org/10.3390/rs8070570

Cerbelaud, A., Roupioz, L., Blanchet, G., Breil, P., Briottet, X. 2021. A repeatable change detection approach to map extreme storm-related damages caused by intense surface runoff based on optical and SAR remote sensing: Evidence from three case studies in the South of France. ISPRS Journal of Photogrammetry and Remote Sensing, 182, 153-175. https://doi.org/10.1016/j.isprsjprs.2021.10.013

Chatziantoniou, A., Petropoulos, G.P., Psomiadis, E. 2017. Co-Orbital Sentinel 1 and 2 for LULC mapping with emphasis on wetlands in a mediterranean setting based on machine learning. Remote Sensing. 9, 1259. https://doi.org/10.3390/rs9121259.

Dabboor, M., White, L., Brisco, B., Charbonneau, F. 2015. Change Detection with Compact Polarimetric SAR for Monitoring Wetlands. Canadian Journal of Remote Sensing, 41, 408–417. https://doi.org/10.1080/07038992.2015.1104634

Gallant, A., Kaya, S., White, L., Brisco, B., Roth, M., Sadinski, W., Rover, J. 2014. Detecting Emergence, Growth, and Senescence of Wetland Vegetation with Polarimetric Synthetic Aperture Radar (SAR) Data. Water, 6, 694–722. https://doi.org/10.3390/w6030694

Haralick, R.M., Shanmugam, K., Dinstein, I. 1973. Textural features for image classificatition. IEEE Transactions on systems, man, and cybernetics. 6, 610–621. https://doi.org/10.1109/TSMC.1973.4309314

Huang, W., Devries, B., Huang, C., Jones, J., Lang, M., Creed, I. 2017. Automated extraction of inland surface water extent from sentinel-1 data. International Geoscience and Remote Sensing Symposium (IGARSS) 2259–2262. https://doi.org/10.1109/ IGARSS.2017.8127439.

Ludwig, C., Walli, A., Schleicher, C., Weichselbaum, J., Riffler, M. 2019. A highly automated algorithm for wetland detection using multi-temporal optical satellite data. Remote Sensing of Environment. 224, 333–351. https://doi.org/10.1016/j.rse.2019.01.017

Mleczko, M., Mróz, M. 2018. Wetland mapping using SAR data from the Sentinel-1A and TanDEM-X missions: a comparative study in the Biebrza Floodplain (Poland). Remote Sensing. 10, 78. https://doi.org/10.3390/rs10010078

Nhangumbe, M., Nascetti, A., Ban, Y. 2023. Multi-Temporal Sentinel-1 SAR and Sentinel-2 MSI Data for Flood Mapping and Damage Assessment in Mozambique. ISPRS International Journal of Geo-Information, 12(2), 53. https://doi.org/10.3390/ijgi12020053

Plank, S., Jüssi, M., Martinis, S., Twele, A. 2017. Combining polarimetric sentinel-1 and ALOS-2/PALSAR-2 imagery for mapping of flooded vegetation. In 2017 IEEE International Geoscience and Remote Sensing Symposium (IGARSS). 5705-5708. IEEE. https://doi.org/10.1109/IGARSS.2017.8128303

Simonow, E. 2020. Uzbekistan dam collapse was a disaster waiting to happen. https:// www.thethirdpole.net/2020/06/23/uzbekistan-dam-collapse/.

Tavus, B., Kocaman, S., Gokceoglu, C., Nefeslioglu, H.A. 2018. Considerations on the Use of Sentinel-1 Data in Flood Mapping In Urban Areas: Ankara (Turkey) 2018 Floods. ISPRS Comm. V Symposium, Int. Arch. Photogramm. Remote Sens.

Spatial Inf. Sci., 42(5), 575-581. https://doi.org/10.5194/isprs-archives-XLII-5-575-2018.

Tavus, B., Kocaman, S., Nefeslioğlu, H., Gökçeoğlu, C. 2019. Flood Mapping Using Sentinel-1 SAR Data: A Case Study of Ordu 8 August 2018 Flood. International Journal of Environment and Geoinformatics, 6(3), 333–337, 2019. https://doi.org/10.30897/ijegeo.666212

Tavus, B., Kocaman, S., Nefeslioglu, H.A., Gokceoglu, C. 2020. A Fusion Approach for Flood Mapping Using Sentinel-1 and Sentinel-2 Datasets. ISPRS Virtual Congress 2020. https://doi.org/10.5194/isprs-archives-XLIII-B3-2020-641-2020

Tavus, B., Kocaman, S., Gokceoglu, C. 2022. Flood damage assessment with Sentinel-1 and Sentinel-2 data after Sardoba dam break with GLCM features and Random Forest method. Science of the Total Environment, 151585. doi.org/10.1016/j.scitotenv.2021.151585

The International Disaster-Emergency Events Database (EMDAT). Disasters Year in Review 2022; Available online: https://www.emdat.be/publications (accessed on 12 April 2022).

Tsyganskaya, V., Martinis, S., Marzahn, P., Ludwig, R. 2018. Detection of temporary flooded vegetation using Sentinel-1 time series data. Remote Sensing. 10, 1286. https:// doi.org/10.3390/rs10081286.

Tsyganskaya, V., Martinis, S., Marzahn, P. 2019. Flood monitoring in vegetated areas using multitemporal Sentinel-1 data: Impact of time series features. Water, 11(9), 1938. https://doi.org/10.3390/w11091938